Nanoscale

PAPER

View Article Online
View Journal

Cite this: DOI: 10.1039/c4nr03661a

Encapsulation of nanoscale metal oxides into an ultra-thin Ni matrix for superior Li-ion batteries: a versatile strategy†

Jianhui Zhu,‡[a,b] Jian Jiang,‡[a,b] Wei Ai,[a] Zhanxi Fan,[c] Xintang Huang,[b] Hua Zhang[c] and Ting Yu*[a,d]

Received 1st July 2014,
Accepted 28th August 2014

DOI: 10.1039/c4nr03661a

www.rsc.org/nanoscale

Li-ion batteries' (LIBs) performance proves to be highly correlated with ionic and electrical transport kinetics in electrodes. Although continual progress has been achieved in rational design of ideal electrode systems, their energy density, cyclic endurance and productivity are still far from perfect for practical use. Herein we propose an interesting, facile and versatile strategy to encapsulate various nanoscale metal oxides (covering both nanopowders and nanostructured arrays) into an ultrathin Ni matrix (metal oxide@Ni) for superior LIBs. Evolutions of such metal oxide@Ni hybrids (taking MnO@Ni and CoO@Ni as models) are thoroughly studied by monitoring their whole fabrication process. Putting "armors" on nanoscale metal oxides is thought helpful for the promotion of the LIB performance since the outer Ni matrix provides both mechanical protection against huge volume changes and effective routes for electron transfer. As a proof-of-concept demonstration, all metal oxide@Ni hybrid electrodes exhibit drastic improvements in the capacity retention (*e.g.* ~452% capacity rise for the MnO@Ni case while ~551% for CoO@Ni NWs), long-term cyclic stability and rate capabilities. This designed strategy can be further extended to make other advanced oxide@metal hybrids, not only for LIBs but also for other potential fields.

1. Introduction

Rapid development in electric vehicles and portable electronics has directed the scientific research to next-generation Li-ion batteries (LIBs) that are required to possess not only endurable cyclic lifespan but also high energy and power densities.[1,2] These battery performances proved to be highly correlated with the transport kinetics of ions and electrons in LIB systems.[3–9] Generally, the optimal electrode kinetics can indeed bring forth several merits involving: (i) improvement of the battery reactivity and reversibility, (ii) maximization of the material utilization and thus enhancement of the energy density, and (iii) dramatic upgrading of the power capability due to shortened pathways for ions diffusion/electron transfer.[6] Up to date, sustained efforts have been dedicated to the optimization of electrode kinetics, by means of engineering electrode materials into well-designed porous structures or creatively making desirable current collectors.[3–9] The original work by Tarascon *et al.* initially demonstrated the achievement of a six-fold increase in power density by building a smart oxide@metal core–shell electrode architecture, with active Fe_3O_4 integrated onto a Cu nanopillar current collector.[7] Follow-up work by Braun *et al.* further updated Tarascon's concept by constructing a series of hybrid electrodes using monolithic three-dimensional (3D) bicontinuous Ni nano-frameworks as conductive backbones, enabling the realization of LIBs with little capacity loss even at ultra-high rates.[8] Recently, Chen *et al.* have developed an intriguing high-rate full battery by immobilizing $Li_4Ti_5O_{12}$/$LiFePO_4$ nanoparticles onto a 3D interconnected, flexible and lightweight graphene foam.[9a] Even though a variety of strategies on establishing advanced electrodes have sprung up, nearly all of them can be categorized into one general concept, that is the incorporation of electrode-active materials with a specific functionalized conductive matrix, normally made from carbons[9] or metals.

Despite that continuous progress has been achieved on electrode kinetic optimization, several formidable challenges are still standing in the way to practical applications. Primarily,

[a]*Division of Physics and Applied Physics, School of Physical and Mathematical Sciences, Nanyang Technological University, 637371, Singapore. E-mail: YuTing@ntu.edu.sg; Fax: +(65) 6795 7981; Tel: +(65) 6316 2962*
[b]*Institute of Nanoscience and Nanotechnology, Department of Physics, Central China Normal University, Wuhan, 430079 Hubei, P.R. China*
[c]*School of Materials Science and Engineering, Nanyang Technological University, 639798, Singapore*
[d]*Graphene Research Centre, National University of Singapore, 117546, Singapore*

† Electronic supplementary information (ESI) available: Experimental details and SEM observations for the hybrids of Fe_3O_4@Ni and C/$CoFeO_x$@Ni NWAs; XRD and SEM/TEM images of ultra-thin $Ni(OH)_2$ nanofilms; XRD and TEM observations on the evolution of the MnO@Ni hybrid; the EDS spectrum and SEM image of Ni films produced from pure ultra-thin $Ni(OH)_2$ nanofilms. See DOI: 10.1039/c4nr03661a

‡ Zhu Jianhui and Jiang Jian contributed equally to this work.

the configuration of nanoscale current collectors into electrode systems inevitably leads to a compromise between the rate capability and specific/volumetric energy densities.[6] Conductive skeletons, in the form of 1D nanowire/nanotube arrays (NWs/NTs) or multi-dimensional bicontinuous networks used for electron transport, usually have occupied too much fraction of volume and weight in electrodes, which gives rise to a low energy density of electrodes per unit area/volume.[10] Addressing this issue by simply filling more active substances into electrodes has yet been considered inadvisable since the overloaded materials would in turn take up the space and channels reserved for electrolyte and ionic diffusion. Next, in general the actives anchored on conducting frameworks are naked and exposed straightforwardly into the electrolyte without any mechanical protections. Upon the deep insertion of Li^+, the high-capacity Li hosts suffering from huge volume expansions tend to become loose and detach from the conducting matrix, which undoubtedly causes severe capacity degradation in long-term cycling.[5] Last but not least, the mass production of such patterned conductive frameworks requires huge expense and complex procedures.[11] Current realization of the metal matrix still relies on the template-assisted electrodeposition technique.[6–8] Though using this approach can generate a diversified array of well-defined periodic architectures,[12] the tedious and costly synthetic procedures pose great difficulties for commercial-scale use. Additionally, unlike conventional powders for thin-film LIBs, the hybrids of monolithic "actives/conductive matrix" show very little promise to be mass-produced on an assembly line.

Trying to overcome above obstacles and produce high-performance anodes for LIBs, we hereby develop a novel and general strategy to encapsulate nanoscale metal oxides into an ultra-thin Ni matrix. The evolution of core–shell oxide@Ni hybrids is thoroughly investigated by monitoring the whole fabrication process. In order to demonstrate the superiority of such metal oxide@Ni hybrids in LIBs, we purposely focused on two representative examples that comprise (i) ultra-long MnO@Ni nanowires (MnO@Ni) as powder models and (ii) CoO@Ni nanowire arrays (CoO@Ni NWs) in a binder-free case. When used for the anode of LIBs, both MnO@Ni and CoO@Ni NWs electrodes exhibit drastic improvements in the capacity retention (*e.g.* ~452% capacity rise in the MnO@Ni case whereas ~551% for CoO@Ni NWs), long-term cyclic stability and rate performance in contrast to the corresponding single-phased oxide counterparts. Our proposed strategy may open up a new prospect on rational design of promising Ni-based composite electrodes for a large spectrum of other potential applications such as electrochemical catalysis and biosensing.

2. Experimental section

Reagents and solvents involved were of analytical grade and used without any additional purification. All chemicals were purchased from Sigma-Aldrich Reagent Co. The typical synthesis of MnO@Ni hybrids and CoO@Ni NWs was listed as follows. To prevent the Ni oxidation, all prepared metal oxide@Ni samples were stored in a vacuum chamber (~10^{-1} MPa). Experimental details for the synthesis of pure $Ni(OH)_2$ ultra-thin films and other metal oxide@Ni hybrids were present in the ESI.†

2.1 Preparation of MnO@Ni hybrids

Ultra-long MnO_2 nanowires were synthesized according to the pioneering literature[13] and directly used as the starting materials. In detail, a mixture of MnO_2 nanowires (0.15 g), hexamethylenetetramine (HMT, 0.7 g), $Ni(NO_3)_2{\cdot}6H_2O$ (0.3 g) and distilled water (50 mL) was treated by ultrasonication for 15 min. The resulting suspension was then transferred into a sealed container (80 mL) and held at 95 °C for 6 h. Afterwards, the intermediate MnO_2@$Ni(OH)_2$ samples were collected and washed with distilled water several times. The preparation of MnO@Ni hybrids was performed in a horizontal, quartz-tube furnace system.[5b,14] 0.3 g MnO_2@$Ni(OH)_2$ powders (pre-dispersed in 10 ml distilled water, dropped onto a ceramic boat and dried at 60 °C) were placed in the centre of a quartz tube (tube diameter: 2 inch). 1.5 mL of ethylene glycol (EG) loaded in an alumina boat was put in the upstream zone of the quartz tube (the distance from the alumina boat to the quartz-tube center: 14 cm). Prior to heating, the tube reactor was sealed and flushed with Ar gas (200 sccm) for 10 min. The furnace was then heated to 620 ± 10 K at a heating rate of ~10 K min^{-1} under a constant Ar flow of 80 sccm, kept for 15 min and allowed to cool down to room temperature naturally.

2.2 Preparation of CoO@Ni NWs

The CoO NWs were made by referring to our previous work[15] and directly used as the raw materials. In brief, a piece of Ti foil with CoO NWs (area: 2.5 × 3.5 cm^2) grown on was immersed into a 80 mL container, wherein there was a 50 mL homogeneous aqueous solution containing 0.15 g $Ni(NO_3)_2{\cdot}6H_2O$ and 0.3 g HMT. Then, the container was sealed and held at 95 °C for 6 h. The obtained products CoO@$Ni(OH)_2$ NWs were fetched out, rinsed and dried at 60 °C. The following reducing treatment was the same as that of the MnO@Ni hybrid except that CoO@$Ni(OH)_2$ NWs took the place of MnO_2@$Ni(OH)_2$.

2.3 Characterization and battery testing

Samples were characterized by powder X-ray diffraction (XRD) (Bruker D-8 Advance), transmission electron microscopy (TEM) (JEOL JEM-2010F) and field-emission scanning electron microscopy (FESEM) (JSM-6700F, 5.0 kV). The capacity values are calculated based on the total mass of electrode materials (exclude carbon black and polymer binders). The mass of electrode materials was measured on a microbalance with an accuracy of 0.01 mg (A&D Company N92, Japan). For powder samples, a conventional slurry-coating process was employed to make the electrodes, which should be finished as quickly as possible. Active material powders, carbon black and poly(vinylidene fluoride) (PVDF) binder were mixed in a mass ratio of 80 : 10 : 10 and homogenized in *N*-methyl-2-pyrrolidone (NMP)

to form slurries. The homogeneous slurries were pasted onto a Cu foil, dried at 90 °C under vacuum for 12 h and cut into electrode discs (diameter: 12 mm). The mass loading of active materials on each current collector was controlled in the range of 1.5–2.8 mg cm^{-2}. Whereas, for the nanostructure array case, the film sample was directly cut into electrode disks and applied as the working electrode, saving the additives and slurry-coating procedures. The mass of metal oxides grown on the current collector was measured within the range of 1.0–1.5 mg cm^{-2}. The coin-type cells (CR2032) were assembled in an Ar-filled glovebox (Mbraun, Unilab, Germany) using the Celgard 2500 membrane as the separator. A Li foil was used as the counter and reference electrodes, and 1 M $LiPF_6$ dissolved in a 1 : 1 (v/v) mixture of ethylene carbonate (EC) and diethyl carbonate (DEC) was utilized as the electrolyte. All cells were aged for 12 h before testing. The discharge–charge cycling was performed at a controlled temperature of 25 ± 0.5 °C using a NEWARE battery tester.

3. Results and discussions

3.1 Material design & working principles

Generally, encapsulating nanoscale metal oxides into an ultra-thin Ni matrix includes two main procedures (Fig. 1). For step I, the pre-synthesized nanostructured oxide precursors are *in situ* wrapped with ultra-thin $Ni(OH)_2$ layers *via* a facile solution method conducted at 95 °C, resulting in the generation of metal oxide@$Ni(OH)_2$ intermediates. This encapsulation is uniform and conformal that nearly all involved oxides are well dispersed/embedded into such a $Ni(OH)_2$ thin-film matrix. Basic characterization of pure $Ni(OH)_2$ film products, composed of X-ray diffraction (XRD) patterns, transmission electron microscopy (TEM), scanning electron microscopy (SEM) and optical observations are presented in Fig. S1.† It is interesting to note that $Ni(OH)_2$ films have a sheet-like morphology and the thickness for one single sheet is estimated to be only around ~7 nm. Step II is a gentle chemical reduction treatment toward the intermediate products, eventually forming the functionalized metal oxide@Ni hybrids. The evolved Ni matrix nearly preserves the geometry of pristine $Ni(OH)_2$ films and still tightly surrounds the inner metal oxides. The sheet-like morphology can be approximately retained at heating temperatures less than 635 K (360 °C). Notice that in the entire fabrication procedures, neither templates nor electrodeposition methods are utilized.

Our synthetic strategy coupled with this special material design concept will bring several highlights as follows:

(I) This strategy is simple and general, capable to be used for mass production of a broad class of core–shell metal oxide@Ni hybrids no matter what forms the oxide precursors are present in. We need to stress that it is applicable for both nanopowders and nanostructured arrays. The only requirement for our typical synthesis is that the core substance can be chemically stable in aqueous solutions and be robust enough to survive in a reduction treatment. By using this method, a series of metal oxide@Ni hybrids like MnO@Ni, Fe_3O_4@Ni, CoO@Ni NWs, C/$CoFeO_x$@Ni nanowall arrays (NWAs) have been fabricated. We believe that the formation of such core–shell hybrid structures is led by simple physical/chemical adsorptions, rather than other possible mechanisms *via* strong chemical bonding, electrostatic adsorption, *etc.*

(II) The introduced conductive matrix is integrated, ultra-thin (~a few nanometers thick), permeable and pretty light-

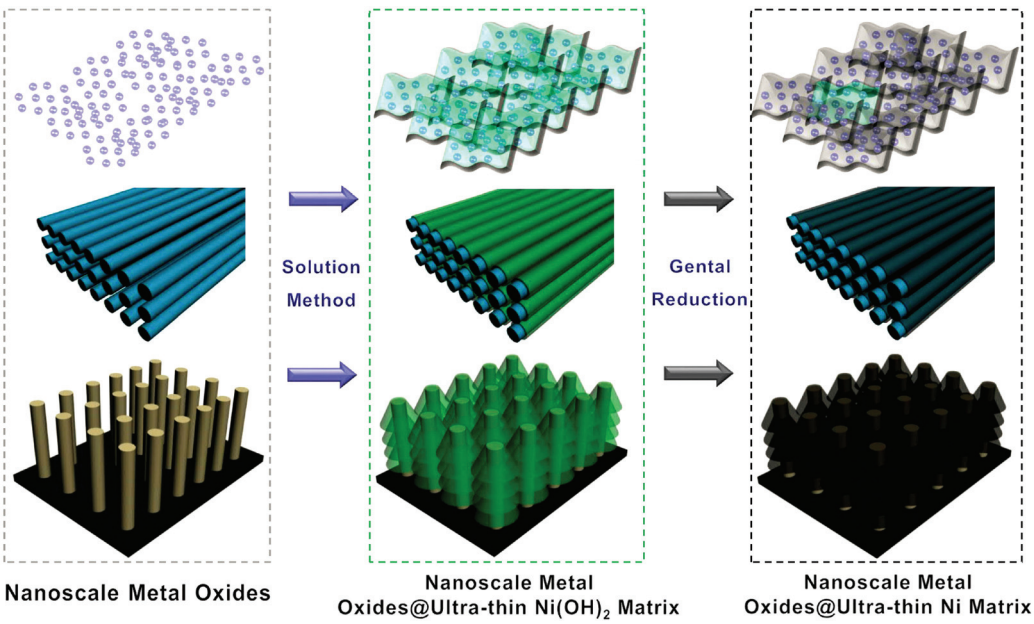

Fig. 1 Schematic showing general procedures of encapsulating various nanoscale metal oxides (covering both nanopowders and nanostructured arrays) into an ultra-thin Ni matrix.

weight as compared to other solid metallic counterparts. In each electrode, Ni films statistically occupy a low proportion in weight (wt% ≤ 19.6%, calculated from the mass difference between original metal oxides and the formed metal oxide@Ni-$(OH)_2$ intermediate), which highly promises the energy density of LIB electrodes.

(III) Ultra-thin Ni layers are uniformly "worn" on nanosized metal oxides. The intimate contacts between the inner oxides and the outer Ni shell facilitate the electron transfer properties. Moreover, upon Li^+ insertion/de-insertion, each individual oxide unit in Ni armor can better accommodate volume changes because the outer surrounded Ni layers are robust and malleable enough to protect the inner actives against the adverse expansion/aggregation effects.

(IV) The manufacture of such a Ni matrix is energy-saving and low-cost as compared to the case of patterned metal frameworks made by tedious electrodeposition, and graphene paradigms obtained *via* chemical or physical energy-consumption routes.

3.2 Evolution & characterization

3.2.1 MnO@Ni nanowires: a typical powder case. We typically chose MnO@Ni nanowires as a model of powder samples to characterize and study the entire evolution process. The raw material of ultra-long MnO_2 nanowires was synthesized according to previous literature.[13] The hydrothermally prepared MnO_2 nanowires possess a mean diameter of ~30 nm and spontaneously form an interwoven architecture (Fig. 2A–C). XRD patterns (Fig. 2S,† bottom) showed the successful generation of α-MnO_2 (JCPDS 81-1947; space group: $I4/m$) with cell parameters of a = 9.78 Å and c = 2.86 Å. After being treated by a solution method, MnO_2 nanowires were then encapsulated within $Ni(OH)_2$ films, forming intriguing coaxial MnO_2@Ni-$(OH)_2$ core–shell hybrid nanostructures (Fig. 2D–F). The newly present diffraction peaks in the XRD pattern (Fig. 2S,† middle) confirm that the generated shell materials belong to α-$Ni(OH)_2$ (JCPDS 22-0752). Note that all MnO_2 nanowires are conformally wrapped with $Ni(OH)_2$ layers, as clearly evidenced by a sharp contrast at the edge of each nanowire in SEM (Fig. 2D) and TEM observations (Fig. S3A–C†). The high-resolution TEM image (Fig. S3C†) definitely uncovers the thickness of the surrounded $Ni(OH)_2$ layer as thin as ~7 nm. The final products of MnO@Ni were further obtained after conducting a gentle reduction toward MnO_2@$Ni(OH)_2$. The derived MnO@Ni hybrid nanowires exactly maintain identical core–shell geometrical morphologies to the intermediate MnO_2@$Ni(OH)_2$ except that the outer Ni shell turns rough. This is quite distinct from former smooth $Ni(OH)_2$ layers (Fig. 2G–I). Though the generated Ni sheets become porous or even turn into nanodots due to complex reduction/interfacial reactions, they still tightly encapsulate the inner MnO nanowires. The hybrid of MnO@Ni shows a mixed XRD pattern of MnO (JCPDS

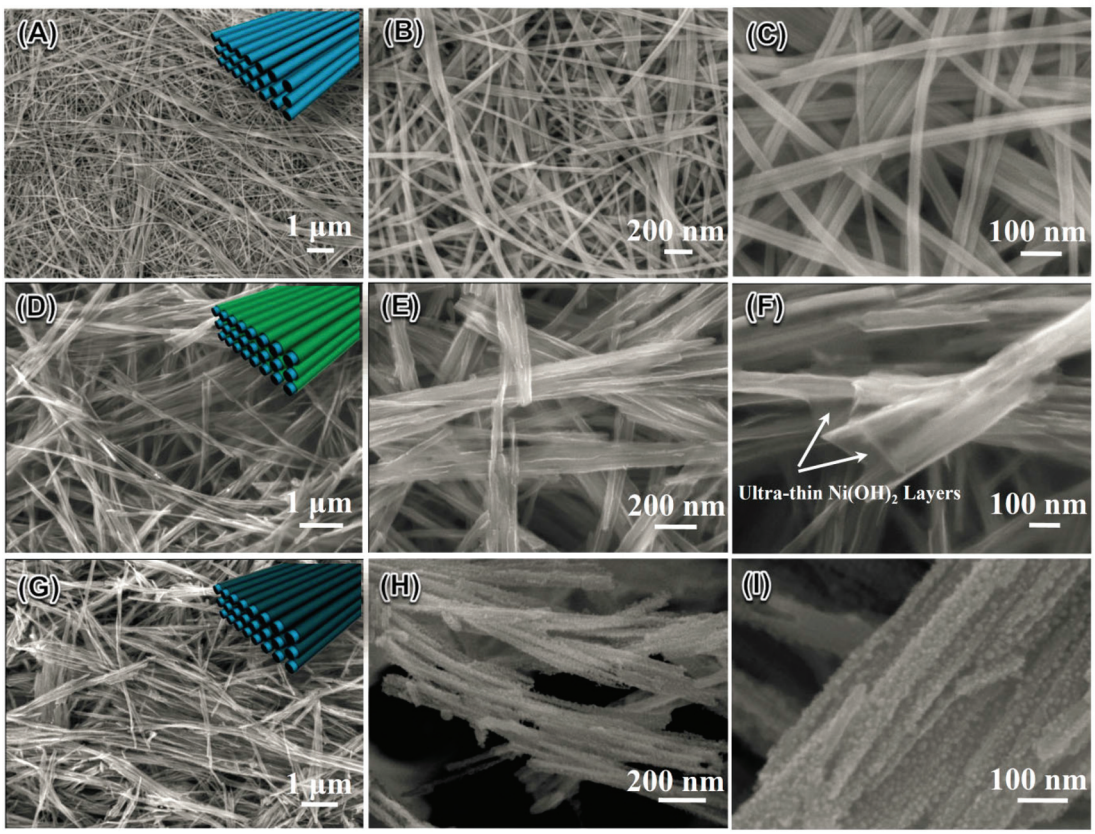

Fig. 2 Representative SEM observations on the evolution of MnO@Ni hybrids: (A–C) ultra-long MnO_2 nanowires, (D–F) the intermediate of MnO_2@$Ni(OH)_2$, (G–I) the ultimate MnO@Ni products.

No. 07-0230) and Ni (JCPDS No. 04-0850) (Fig. 2S,† top); no other diffraction peaks from possible impurities (*e.g.*, NiO, *etc.*) were detected, confirming the total transformation of MnO_2 to MnO and the complete reduction of $Ni(OH)_2$ to Ni. The EDS spectrum of MnO@Ni hybrids (Fig. S4a†) reveals that the Mn/Ni atom ratio is 2.9 : 1 corresponding to a Ni content of ~22% (quite close to our result of 19.6% aforementioned). Moreover, EDS and SEM measurements on pure Ni nanofilms (evolved from the same $Ni(OH)_2$ precursor) were also performed to ensure this reduction conversion (see Fig. S4b†). The EDS result evidently shows that Ni is present in a huge proportion (the Ni : O ratio is close to 19 : 1) in the reduced products. The slight impurity of C and O may largely come from the remaining ethylene glycol or other yielded by-products (*e.g.* *R*-OH, *R*-COH, *R*-COOH, *etc.*), which could be readily understandable since the reduction procedure was undertaken in an organic atmosphere.

Let us concentrate on detailed structural features of MnO@Ni core–shell products. SEM (Fig. 3A) and TEM (Fig. 3D) images illustrate that the evolved MnO@Ni hybrid nanowires are still kept interwoven with each other, forming an integrated network-like film structure. Closer inspections (Fig. 3B and C) disclose that there distributed numerous interconnected nanoparticles on the surface of MnO@Ni. High-resolution TEM observation on the selected region reveals that the outer skin of the MnO@Ni hybrid has a polycrystalline nature (Fig. 3E). Distinct lattice fringes with interplanar spacings of 0.2 nm and 0.17 nm successively match well with the (111) and (200) facets of cubic Ni. The formation of a defective/porous Ni film, rather than a conformal Ni layer, may result from the thermal decomposition of $Ni(OH)_2$ and possible solid-state interfacial diffusions/reactions between NiO_x and MnO. Similar phenomena and relevant mechanisms among adjacent materials have been elaborated in pioneering work.[16] Such defects on the MnO@Ni surface can facilitate Li^+ ion access to the inner MnO and accordingly favor the high-rate lithiation/delithiation. In the inner part of the MnO@Ni nanowire (Fig. 3F), the lattice fringe of 0.26 nm corresponds to the (111) plane of manganosite MnO, which is highly in accordance with the XRD result and in the meantime indicates that the derived MnO core can still preserve a high crystalline property though subjected to a reduction procedure. Fig. 3H–J display the energy dispersive X-ray spectroscopy (EDX) elemental mapping toward the designated region (Fig. 3G), verifying the supposed hybrid composition of MnO@Ni and the uniform encapsulation of Ni layers.

Another hybrid of Fe_3O_4@Ni was successfully made by following the same steps but starting with the precursor of single-crystalline Fe_3O_4 hexagonal nanoplates (~60–100 nm in width and ~10 nm in thickness).[17] Clearly, almost each of Fe_3O_4 nanoplates has been packed within the integrated ultrathin Ni film matrix (Fig. S5†). This designed core–shell hybrid

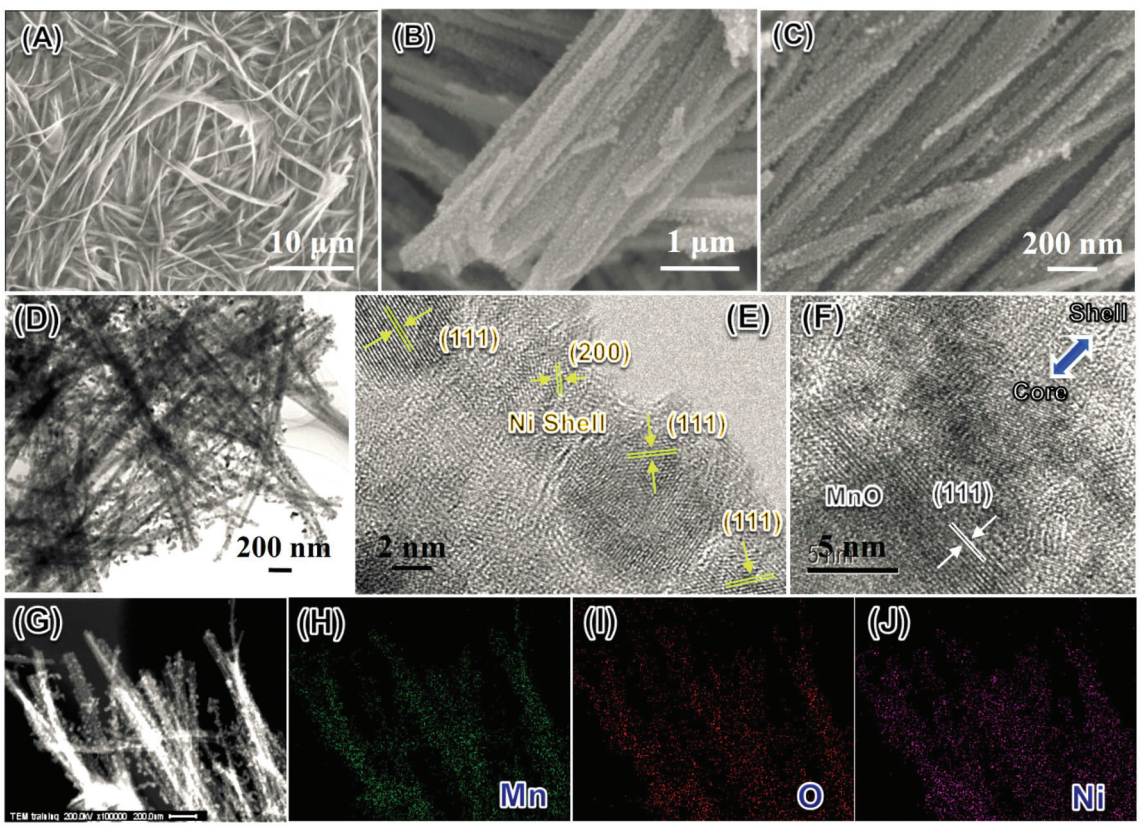

Fig. 3 Electron microscopy characterization: (A–C) SEM and (D) TEM images of evolved MnO@Ni hybrids; (E–F) high-resolution TEM observations toward their outer shell and inner core structures, respectively; (G–J) EDX elemental mapping of core–shell MnO@Ni hybrid products.

electrode architecture is fairly interesting and considered favorable for LIB applications. The whole fabrication procedure is controllable; the mass fraction of Ni in ultimate powder samples can be precisely controlled by tuning the additional amount of Ni salts in the initial hydrothermal process. We need to emphasize that these uniform hybrid powders of the metal oxide@Ni matrix can hardly be realized by conventional electrodeposition techniques, unambiguously reflecting that our present methodology is pretty unique, efficient and smart.

3.2.2 CoO NW@Ni: an example of arrayed nanostructures. This synthetic protocol is also applicable for making various arrayed metal oxide@Ni nanostructures. Herein, mesoporous CoO NWs grown on Ti foils are taken as typical examples because they have long been used as "hot" building blocks to construct 3D synergetic core–shell/branch hybrid films for electrochemical energy storage devices.[2c,16c,18,19] The precursor of CoO NWs with a diameter range of ~60–80 nm was fabricated according to our previous work (Fig. 4A–C).[15] After undergoing a simple soaking process, the yielded ultra-thin $Ni(OH)_2$ films were surrounded homogeneously on each CoO nanowire to form the core–shell hybrid of CoO@$Ni(OH)_2$ NWs (Fig. 4D–F). Note that such thin $Ni(OH)_2$ films connect the neighboring CoO nanowires closely with each other. CoO@Ni NWs were finally produced after a mild reduction process. As clearly observed (Fig. 4G–I), the products well inherited the geometric morphologies of CoO@$Ni(OH)_2$ NWs. The Ni shells with a smooth and conformal structure are still firmly coated on CoO NWs. The crystal structure and phase purity of hybrid CoO@Ni NWs were examined by XRD (Fig. S6†). In XRD patterns, an overlapped diffraction pattern of cubic CoO (JCPDS no. 48-1719) and Ni well testifies the establishment of core–shell CoO@Ni NWs on the Ti substrate. TEM characterization was further performed to elucidate the structural features of CoO@Ni NWs (Fig. 5A–C). The arrayed mesoporous CoO nanowires are totally encircled by the thin Ni overwrap. The CoO core and Ni shell can be readily distinguished from the designated region in Fig. 5B. The lattice with an interplanar spacing of ~0.21 nm in the core section is indexed to the (200) facet of CoO while lattice fringes with a spacing distance of ~0.2 nm emerging at the outward shell are in good agreement with the (111) plane of Ni. This high-resolution TEM image also evidences the intimate contact between the inner CoO core and the outer Ni shell. The EDX mapping analysis on the selected area (Fig. 5D–G) discloses the elemental distribution of CoO@Ni NWs and definitely confirms their hierarchical core–shell hybrid structure.

In addition to the encapsulation of CoO NWs into the Ni matrix, our developed approach can be extended to fabricate other metal oxide@Ni core–shell nanostructure arrays. For instance, C/$CoFeO_x$@Ni NWAs composed of C/$CoFeO_x$NWA cores[20] and Ni shells have been built successfully by adopting

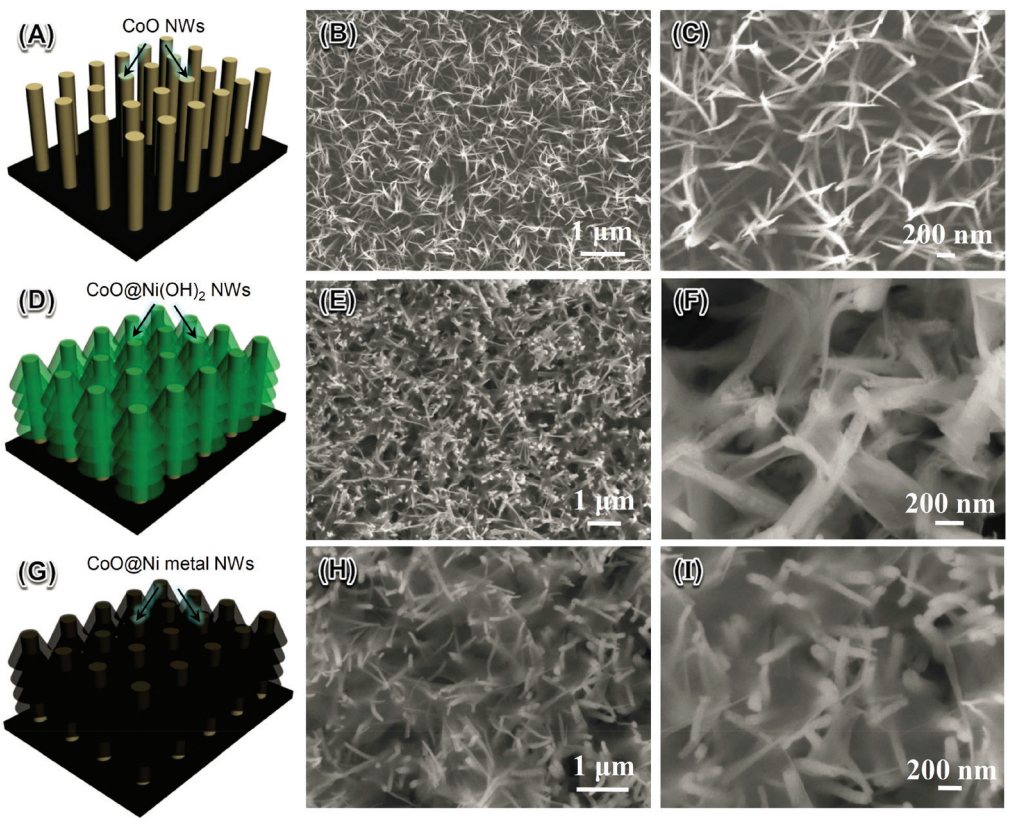

Fig. 4 Representative SEM observations on the evolution of CoO@Ni hybrid NWs: (A–C) pristine CoO NWs grown on Ti foil; (D–F) the CoO@Ni-$(OH)_2$ intermediate; (G–I) the ultimate CoO@Ni NWs.

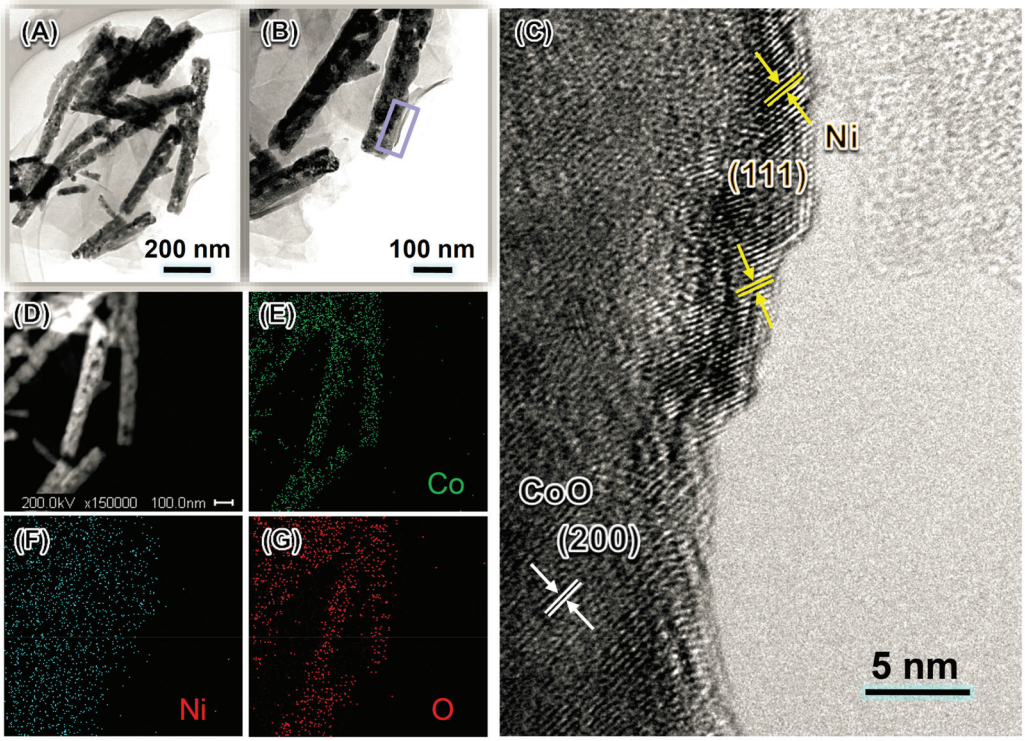

Fig. 5 Electron microscopy characterization: (A–B) TEM, (C) HRTEM observations and (D–F) EDX elemental mapping toward the evolved CoO@Ni hybrid NWs.

the same evolution method. The overall morphology/architecture of derived C/$CoFeO_x$@Ni NWAs is similar to that of CoO@Ni NWs, with veil-like thin Ni films covering on each individual nanowall surface (Fig. S7†). Compared to previously synthesized metal oxides@metal core–shell/branch nanostructure arrays by means of electrodeposition,[21] our synthetic approach is more easy to operate (without any electrochemical equipment and related accessories), cost-effective and energy-saving.

3.3 LIB properties of metal oxide@Ni hybrids

The encapsulation of nanoscale metal oxides into an ultra-thin Ni matrix renders this system very intriguing for LIB applications. The anodic performance of MnO@Ni nanowires was evaluated for the powder case study. Fig. 6A compares the cyclic behaviors between pure MnO nanowires and MnO@Ni core–shell products at a current density of ~350 mA g^{-1}. Pure MnO nanowires exhibit a very poor cyclic behavior. Within the first 40 cycles, their specific discharge capacity descends sharply from the top ~1387 mA h g^{-1} down to the value of ~200 mA h g^{-1}; even worse, only a very poor capacity of ~119 mA h g^{-1} is preserved after 250 cycles. The drastic capacity degradation is mainly caused by the structural pulverization of such fine MnO nanowires. By contrast, the MnO@Ni hybrid still maintains a specific capacity of ~655 mA h g^{-1} after 250 deep cycles, enabling a large capacity rise of +452% compared to that of single-phase MnO nanowires. Particularly noteworthy is an interesting and curious phenomenon that the capacity of MnO@Ni initially drops to the bottom of ~478 mA h g^{-1} (recorded at the 64th cycle) but later progressively recovers to ~658 mA h g^{-1} (no similar capacity-rise occurs in the pure MnO nanowire case). To study in depth the electrochemical properties of the MnO@Ni electrode and better understand this capacity-rise phenomenon, we intentionally investigated the charge/discharge curves (Fig. 6B) and analyzed their corresponding differential capacity (dQ/dV) plots at the 10th, 30th, 64th, 120th, 160th and 200th cycle, respectively (Fig. 7). During the 1st discharge, the voltage decreases steeply from the open-circuit value to ~0.49 V where a plateau region sets in and continues until a capacity of ~1248 mA h g^{-1} is achieved. In the reverse charge (polarization) process, there are two plateaus successively present at ~1.29 V and ~2.23 V due to complex phase transformations of Mn^0/MnO_x,[22] contributing a total charge capacity of ~928 mA h g^{-1} and a high initial Coulombic efficiency up to ~74.4%. After 10 cycles, the electrode of the MnO@Ni hybrid still shows analogous polarization/de-polarization behaviors to the 1st one, with a cathodic peak located at ~0.48 V and two anodic peaks at ~1.31 V and ~1.98 V, respectively (Fig. 7A). Over 30 cycles, the obvious decline in anodic peak intensity (Fig. 7B and C) declares the onset of capacity decay. We believe that the capacity fading, to a great extent, may stem from the disruption or local structural rearrangements of MnO nanowires during lithiation/delithiation processes.[22] In the dQ/dV plot of the 64th cycle both cathodic and anodic peaks turn weak (or even vanished), which is in agreement with the cyclic result that the hybrid electrode runs

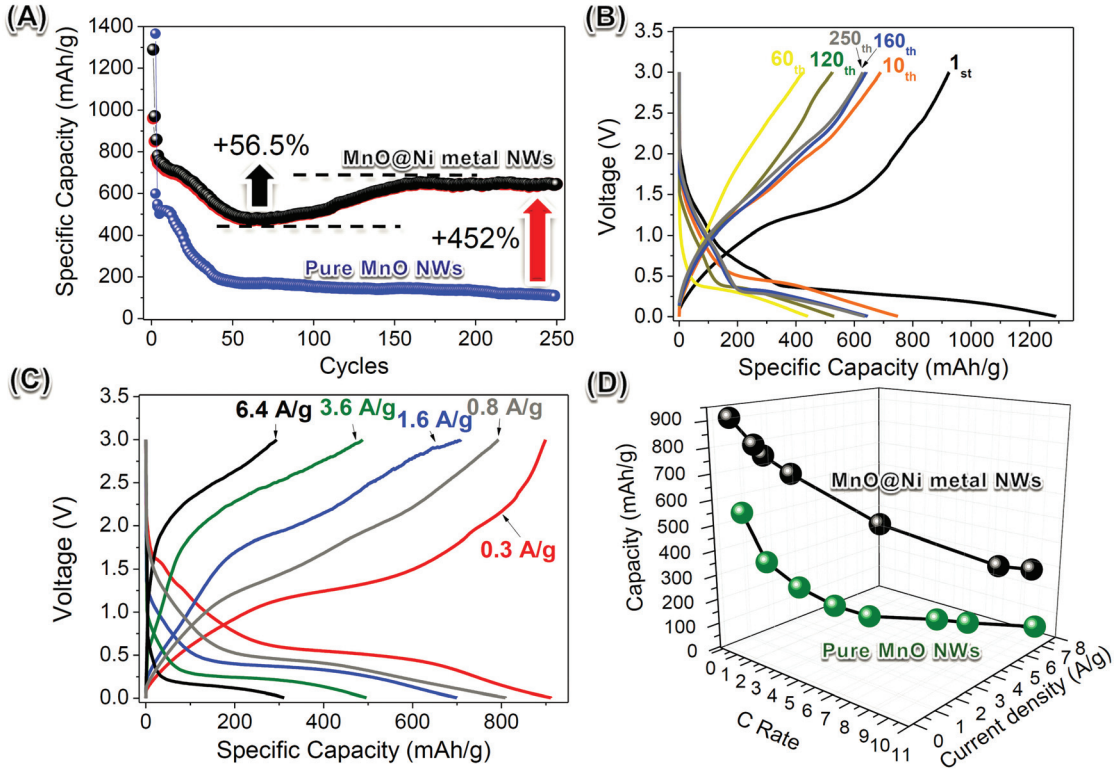

Fig. 6 (A) Cyclic comparison of MnO@Ni hybrids and pure MnO nanowires at a current density of ~350 mA g^{-1}. (B) Charge/discharge curves of MnO@Ni in the voltage range of 0.005–3 V at a constant current rate of ~350 mA g^{-1}. (C) Charge/discharge curves of MnO@Ni performed at varied current densities. (D) Comparison of the rate performance between MnO@Ni hybrids and pure MnO nanowires.

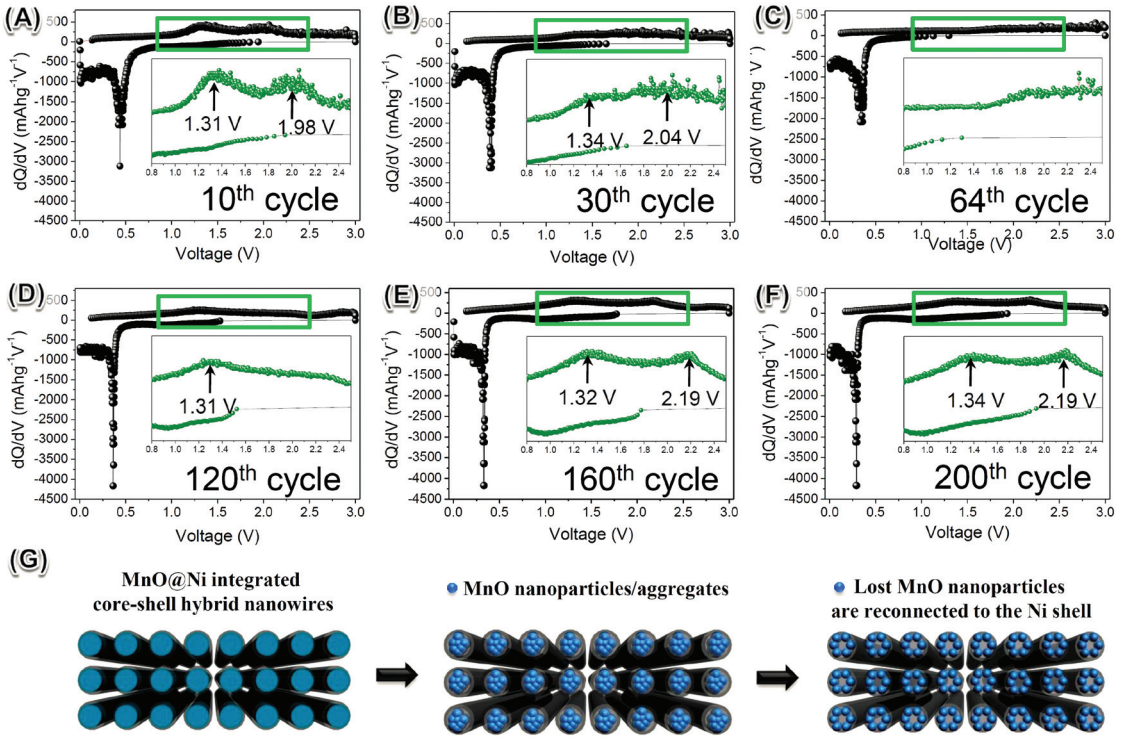

Fig. 7 (A–F) Corresponding differential capacity plots (d*Q*/d*V*) of the MnO@Ni hybrid electrode at the 10th, 30th, 64th, 120th, 160th and 200th cycle, respectively. (G) A proposed schematic showing the electrochemical reaction mechanism of the MnO@Ni hybrid electrode.

at the lowest capacity. Afterwards, the charge/discharge capacity starts to revive in subsequent cycles. The delivered capacity increases up to ~532 mA h g^{-1} (at the 120th cycle), with a high growing rate of ~1 mA h g^{-1} per cycle. Note the fact that one polarization peak related to Mn^0/Mn^{2+} conversion re-emerges at the potential of ~1.31 V suggesting a partial recovery of anodic reactions (Fig. 7D).[22a] The capacity of the MnO@Ni electrode continually grows to a maximum value of ~658 mA h g^{-1} at the 160th cycle and remains stabilized around 655 m Ah g^{-1} in later cycles. The dQ/dV plots in Fig. 7E and F show the regeneration of two anodic polarization peaks at ~1.3 V and ~2.19 V, respectively. Peak positions are overall similar to the case of the 10th cycle though one of anodic peaks has a slight potential shift (~0.21 V) from ~1.98 V to the positive direction. On the basis of experimental records and analysis above, the proposed electrochemical process (Fig. 7G) may account for the origin of energy-storage recovery. MnO nanowires in the MnO@Ni core–shell hybrid primarily convert into amorphous MnO nanoparticles owing to inevitable structural destructions including lattice distortions, substantial volume expansions, pulverization and particle aggregations *etc.* This Li-storage mechanism for MnO and other transitional metal oxides has been well accepted and demonstrated in pioneering work.[22–25] These adverse factors stepwise bring forth electrical connection losses and irreversible capacity especially in the range of 24–64 cycles (Fig. 6A and B). However, along with consecutive cycling those MnO nanoparticles that originally lost electronic contacts are capable of reconnecting with the Ni shell progressively (as proved by the gradual enhancement in the intensity of MnO anodic peaks), thereby giving rise to an unusual capacity revival. During this period, the robust, malleable and ultra-thin Ni "armors" worn on MnO nanowires play a vital role, not only in the accommodation of volume changes led by Li ion insertion/extraction but also in protecting them against aggregation effects and foremost favoring the uniform dispersion and capacity recovery of MnO actives. This highly guarantees excellent electrochemical stability and prolonged cyclic lifetime in contrast to the bare MnO nanowires. Additionally, SEM and TEM observations were carried out purposely on the MnO@Ni electrode after 250 cycles (Fig. S8†). Despite the fatigue working of electrodes, we can still distinctly find the trace of MnO@Ni nanowires. It is worth noting that as a result of Li^+ insertion/de-insertion, the pristine solid core–shell MnO@Ni hybrids change into cave-distributed nanowires or even interior hollow "nanotubes" with a tube thickness of ~20 nm (far higher than ~7 nm). This verifies the truth of MnO nanowires breaking up into dispersive nanoparticles upon cycling. Besides, the formation of thicker tubular walls is highly in favor of our proposed electrochemical mechanism wherein tiny MnO nanoparticles would re-gather/re-contact to Ni shells leading to the capacity revival.

Fig. 6C and D show the rate performance of the MnO@Ni electrode conducted at varied current densities from 0.3 A g^{-1} to 6.4 A g^{-1}. For comparison, the relationship between current rates *versus* the capacity of pure MnO nanowires is also present. The electrode of MnO@Ni shows superior specific capacities and rate behaviors to the pure MnO nanowire electrode. At a low current rate of 0.3 A g^{-1}, the MnO@Ni electrode exhibits a reversible specific capacity of ~916 mA h g^{-1}, far higher than the maximum of MnO nanowires (~550 mA h g^{-1}). With the increase of current densities, the hybrid electrode can deliver capacities up to ~810 mA h g^{-1} (0.8 A g^{-1}), ~701 mA h g^{-1} (1.6 A g^{-1}), ~502 mA h g^{-1} (3.6 A g^{-1}) and ~326 mA h g^{-1} (6.4 A g^{-1}), respectively (Fig. 6C). The enhancement of rate capability mainly derives from the improved electrochemical reversibility/activity and reaction kinetics induced by the Ni matrix. On the one hand, the outer Ni shell tightly packing the inner active materials promises the reversible Li storage of MnO and substantially maximizes the electrochemical utilization. On the other hand, the powerful Ni armor makes electrode materials still preserve a unique 1D hybrid nano-architecture. This configuration effectively enables rapid electron transfer from MnO active sites to the external circuit along conductive "electric cables",[26] as confirmed by the electrochemical impedance spectroscopy (EIS) testing (Fig. S9†).

In parallel, we also studied the LIB performance of CoO@Ni NWs for the binder-free example. Fig. 8A shows the comparison of pure CoO NWs and CoO@Ni NWs for cyclic stability. In the initial charge/discharge cycle, the capacities of CoO@Ni NWs are recorded around ~813 mA h g^{-1} and ~968 mA h g^{-1}, respectively, with a high initial Coulombic efficiency of 83.9%. Pure mesoporous CoO NWs nearly possess the same electrochemical properties, exhibiting charge/discharge capacities of ~810 mA h g^{-1} and ~953 mA h g^{-1} (Coulombic efficiency: ~84.9%). However, the bare CoO NWs unfortunately retain a very low capacity of ~110 mA h g^{-1} after 100 cycles. Their poor capacity retention is mainly ascribed to certain factors like the fracture/collapse of nanowires and adverse aggregation of newly generated amorphous CoO nanoparticles upon deep cycling. This might be fully understandable on account of the intrinsic texture of "nanoparticle-interconnected" CoO NWs.[15] By sharp contrast, the hybrid of CoO@Ni NWs shows a remarkable capacity rise of +551% which can still maintain a specific capacity as high as ~789 mA h g^{-1} over 100 cycles. The capacity retention even reaches ~97% relative to the initial reversible discharge value. The corresponding charge/discharge curves of CoO@Ni NWs (Fig. 8B) show a much higher discharge plateau (centered at ~1.2 V) and a lower charge plateau (at ~2.0 V) than nanosized CoO in reported studies,[15,27] revealing that such a CoO@Ni hybrid configuration has less potential hysteresis and smaller internal resistance. Rate capabilities of CoO@Ni NWs were examined at varied current rates (Fig. 8C and D). Along with the current density increase from ~150 to 4800 mA g^{-1}, CoO@Ni NWs exhibit stable capacities varying at 839 (150 mA g^{-1}), 788 (300 mA g^{-1}), 728 (600 mA g^{-1}), 665 (1200 mA g^{-1}), 534 (2400 mA g^{-1}) and 356 mA h g^{-1} (4800 mA g^{-1}), respectively. All these values are definitely larger than those of pure CoO NWs. The noticeable improvements in rate behaviors show the positive cooperative effects between the ionic conducting mesoporous CoO NWs and the electronic conductive Ni shells. Apart from CoO@Ni NWs, C/$CoFeO_x$@Ni NWAs

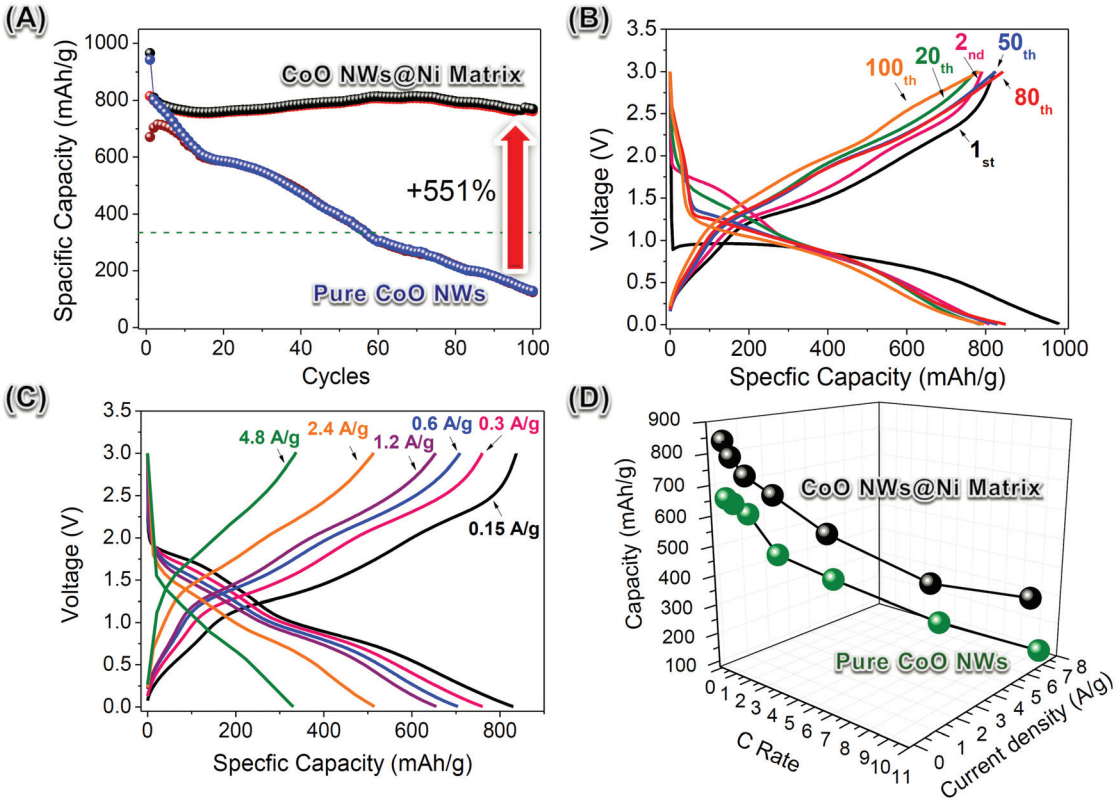

Fig. 8 (A) Cyclic comparison of pristine CoO NWs and CoO@Ni NWs at a current density of ~300 mA g^{-1}. (B) Charge/discharge curves of CoO@Ni NWs in a voltage window of 0.005–3 V at ~300 mA g^{-1}. (C) Charge/discharge curves of CoO@Ni NWs at varied current densities; (D) comparison of rate capabilities between CoO@Ni NW and bare CoO NW electrodes.

shows success in LIB performance promotions by integrating an ultra-thin Ni matrix with C/$CoFeO_x$ NWAs (see detailed electrochemical testing information in Fig. S10†). This example once again highlights our clever encapsulation concept for electrochemical energy-storage applications.

4. Conclusions

In summary, we developed a facile and versatile strategy for encapsulating nanoscale metal oxides into an ultra-thin Ni matrix for superior LIB application. The outer thin Ni shells acting like robust armors can provide mechanical protection to inner metal oxides against detrimental volume changes and also provide highly conductive pathways for charge transfer. For demonstration, MnO@Ni hybrid nanowires (for powder case) and CoO@Ni NWs (for binder-free example) were chosen as two distinct prototypes to study the overall structural evolutions and the anodic performances in LIBs. When evaluated as the anode of LIBs, the hybrid of MnO@Ni shows remarkably improved energy-stored capability (~452% rise in specific capacity), superior rate behavior and cyclic stability to bare MnO nanowire electrodes. Also, the CoO@Ni NW electrode exhibits drastic improvement in capacity retention (~551% increase), rate and long-term cyclic performance when compared to the single-phase CoO counterpart. Our present strategy is general, powerful, simple and effective, suitable for both the construction of functional hybrid nanostructured arrays and fabrication of complex oxide@metal core–shell heterostructured nanoparticles that can be hardly achieved *via* conventional electrodeposition routes. This work may also set up a new platform to develop more state-of-the-art oxide@metal core–shell hybrids for advanced applications, not merely in LIBs but also in other electrochemical and environmental fields.

Acknowledgements

This work was supported by the Singapore National Research Foundation under NRF-RF award No. NRF-RF2010-07, A*Star SERC PSF grant 1321202101 and MOE Tier 2 MOE2012-T2-2-049. Prof. H. Zhang thanks the support from MOE under AcRF Tier 2 (ARC 26/13, No. MOE2013-T2-1-034), AcRF Tier 1 (RG 61/12, RGT18/13, RG5/13), and Start-Up Grant (M4080865.070.706022) in Singapore. This research is also conducted by the NTU-HUJ-BGU Nanomaterials for Energy and Water Management Programme under the Campus for Research Excellence and Technological Enterprise (CREATE), which is supported by the National Research Foundation, Prime Minister's Office, Singapore.

Notes and references

1 (*a*) P. G. Bruce, B. Scrosati and J.-M. Tarascon, *Angew. Chem., Int. Ed.*, 2008, **47**, 2930; (*b*) J.-M. Tarascon and M. Armand, *Nature*, 2001, **414**, 359.

2 (*a*) B. Kang and G. Ceder, *Nature*, 2009, **458**, 190; (*b*) X. Lai, J. E. Halperta and D. Wang, *Energy Environ. Sci.*, 2012, **5**, 5604; (*c*) W. Zhou, J. Zhu, C. Cheng, J. Liu, H. Yang, C. Cong, C. Guan, X. Jia, H. Fan, Q. Yan, C. M. Li and T. Yu, *Energy Environ. Sci.*, 2011, **4**, 4954.

3 (*a*) J. Liu, G. Cao, Z. Yang, D. Wang, D. Dubois, X. Zhou, G. L. Graff, L. R. Pederson and J. Zhang, *ChemSusChem*, 2008, **1**, 676; (*b*) J. H. Liu, J. S. Chen, X. F. Wei, X. W. Lou and X. W. Liu, *Adv. Mater.*, 2011, **23**, 998; (*c*) D. R. Rolison, J. W. Long, J. C. Lytle, A. E. Fischer, C. P. Rhodes, T. M. McEvoy, M. E. Bourga and A. M. Lubers, *Chem. Soc. Rev.*, 2009, **38**, 226.

4 (*a*) W. Wang, M. Tian, A. Abdulagatov, S.-M. George, Y.-C. Lee and R.-G. Yang, *Nano Lett.*, 2012, **12**, 655; (*b*) Y. Yu, L. Gu, X.-Y. Lang, C.-B. Zhu, T. Fujita, M.-W. Chen and J. Maier, *Adv. Mater.*, 2011, **23**, 2443; (*c*) Y. Fu, Z. Yang, X. Li, X. Wang, D. Liu, D. Hu, L. Qiao and D. He, *J. Mater. Chem. A*, 2013, **1**, 10002.

5 (*a*) J. Jiang, Y. Li, J. Liu, X. Huang, C. Yuan and X. W. Lou, *Adv. Mater.*, 2012, **24**, 5166; (*b*) J. Jiang, J. Zhu, Y. Feng, J. Liu and X. Huang, *Chem. Commun.*, 2012, **48**, 7471; (*c*) J. Zhu, J. Jiang, Y. Feng, G. Meng, H. Ding and X. Huang, *ACS Appl. Mater. Interfaces*, 2013, **5**, 2634; (*d*) C. X. Zhai, N. Du, H. Zhang and D. R. Yang, *Chem. Commun.*, 2011, **47**, 1270.

6 S. Chabi, C. Peng, D. Hu and Y. Zhu, *Adv. Mater.*, 2014, **26**, 2440.

7 P.-L. Taberna, S. Mitra, P. Poizot, P. Simon and J.-M. Tarascon, *Nat. Mater.*, 2006, **5**, 567.

8 (*a*) H.-G. Zhang, X.-D. Yu and P.-V. Braun, *Nat. Nanotechnol.*, 2011, **6**, 277; (*b*) J. H. Pikul, H. G. Zhang, J. Cho, P. V. Braun and W. P. King, *Nat. Commun.*, 2013, **4**, 1732; (*c*) H. Zhang and P. V. Braun, *Nano Lett.*, 2012, **12**, 2778.

9 (*a*) N. Li, Z. Chen, W. Ren, F. Li and H.-M. Cheng, *Proc. Natl. Acad. Sci. U. S. A.*, 2012, **109**, 17360; (*b*) J. Luo, J. Liu, Z. Zeng, C. F. Ng, L. Ma, H. Zhang, J. Lin, Z. Shen and H. J. Fan, *Nano Lett.*, 2013, **13**, 6136; (*c*) H. Ji, D. P. Sellan, M. T. Pettes, X. Kong, J. Ji, L. Shi and R. S. Ruoff, *Energy Environ. Sci.*, 2014, **7**, 1185; (*d*) H. Ji, L. Zhang, M. T. Pettes, H. Li, S. Chen, L. Shi, R. Piner and R. S. Ruoff, *Nano Lett.*, 2012, **12**, 2446; (*e*) M. Yan, F. Wang, C. Han, X. Ma, X. Xu, Q. An, L. Xu, C. Niu, Y. Zhao, X. Tian, P. Hu, H. Wu and L. Q. Mai, *J. Am. Chem. Soc.*, 2013, **135**, 18176.

10 R. Liu, J. Duay and S. Lee, *Chem. Commun.*, 2011, **47**, 1384.

11 J. Jiang, Y.-Y. Li, J.-P. Liu and X.-T. Huang, *Nanoscale*, 2011, **3**, 45.

12 M. Fu, K. Chaudhary, J. G. Lange, H. S. Kim, J. Juarez, J. A. Lewis and P. V. Braun, *Adv. Mater.*, 2014, **26**, 1740.

13 (*a*) X. Wang and Y. Li, *J. Am. Chem. Soc.*, 2002, **124**, 2880; (*b*) B. Lan, L. Yu, T. Lin, G. Cheng, M. Sun, F. Ye, Q. Sun and J. He, *ACS Appl. Mater. Interfaces*, 2013, **5**, 7458.

14 (*a*) J. Jiang, J. Liu, W. W. Zhou, J. H. Zhu, X. T. Huang, X. Y. Qi, H. Zhang and T. Yu, *Energy Environ. Sci.*, 2011, **4**, 5000; (*b*) C. Zhou and J. P. Liu, *Nanotechnology*, 2014, **25**, 035402.

15 J. Jiang, J. P. Liu, R. M. Ding, X. X. Ji, Y. Y. Hu, X. Li, A. Z. Hu, F. Wu, Z. H. Zhu and X. T. Huang, *J. Phys. Chem. C*, 2010, **114**, 929.

16 (*a*) R. Mukherjee, T. Chakrabarti, E. A. Anumol, T. A. Abinandanan and N. Ravishankar, *ACS Nano*, 2011, **5**, 2700; (*b*) E. Anumol, B. Viswanath, P. Ganesan, Y. F. Shi, G. Ramanath and N. Ravishankar, *Nanoscale*, 2010, **2**, 1423; (*c*) J. Jiang, J. Luo, J. Zhu, X. Huang, J. Liu and T. Yu, *Nanoscale*, 2013, **5**, 8105.

17 M. Ma, Y. Zhang, Z. Guo and N. Gu, *Nanoscale Res. Lett.*, 2013, **8**, 16.

18 (*a*) J. Liu, J. Jiang, C. W. Cheng, H. X. Li, J. X. Zhang, H. Gong and H. J. Fan, *Adv. Mater.*, 2011, **23**, 2076; (*b*) C. Guan, J. P. Liu, C. W. Cheng, H. X. Li, X. L. Li, W. W. Zhou, H. Zhang and H. J. Fan, *Energy Environ. Sci.*, 2011, **4**, 4496; (*c*) X. Xia, C. Zhu, J. Luo, Z. Zeng, C. Guan, C. F. Ng, H. Zhang and H. J. Fan, *Small*, 2014, **10**, 766.

19 C. Zhou, Y. Zhang, Y. Li and J. Liu, *Nano Lett.*, 2013, **13**, 2078.

20 J. Jiang, J. Zhu, R. Ding, Y. Li, F. Wu, J. Liu and X. Huang, *J. Mater. Chem.*, 2011, **21**, 15969.

21 X. Xia, Q. Xiong, Y. Zhang, J. P. Tu, C. F. Ng and H. J. Fan, *Small*, 2014, **10**, 2419.

22 (*a*) S. Wang, Y. Ren, G. Liu, Y. Xing and S. Zhang, *Nanoscale*, 2014, **6**, 3508; (*b*) X. Li, D. Li, L. Qiao, X. Wang, X. Sun, P. Wang and D. He, *J. Mater. Chem.*, 2012, **22**, 9189; (*c*) H. Xia, M. Lai and L. Lu, *J. Mater. Chem.*, 2010, **20**, 6896; (*d*) K. Zhong, X. Xia, B. Zhang, H. Li, Z. Wang and L. Chen, *J. Power Sources*, 2010, **195**, 3300.

23 J.-M. Tarascon and M. Armand, *Nature*, 2008, **451**, 652.

24 P. Poizot, S. Laruelle, S. Grugen, L. Dupont and J. M. Tarascon, *Nature*, 2000, **407**, 496.

25 (*a*) L. Li, A.-R. O. Raji and J. M. Tour, *Adv. Mater.*, 2013, **25**, 6298; (*b*) J. Lin, A.-R. O. Raji, K. Nan, Z. Peng, Z. Yan, E. L. G. Samuel, D. Natelson and J. M. Tour, *Adv. Funct. Mater.*, 2014, **24**, 2044; (*c*) W. Zhou, Y. Tay, X. Jia, D. Wai, J. Jiang, H. Hoon and T. Yu, *Nanoscale*, 2012, **4**, 4459.

26 F. F. Cao, J. W. Deng, S. Xin, H. X. Ji, O. G. Schmidt, L. J. Wan and Y. G. Guo, *Adv. Mater.*, 2011, **23**, 4415.

27 (*a*) L. Zhu, Z. Wen, W. Mei, Y. Li and Z. Ye, *J. Phys. Chem. C*, 2013, **117**, 20465; (*b*) J. Do and C. Weng, *J. Power Sources*, 2006, **159**, 323; (*c*) L. Zhang, P. Hu, X. Zhao, R. Tian, R. Zou and D. Xia, *J. Mater. Chem.*, 2011, **21**, 1827.